Quantitative thermomechanical characterisation of 3D-woven SiC/SiC composites from in-situ tomographic and thermographic imaging

Léonard Turpin, Stéphane Roux, Jean Bénézech, Guillaume Couégnat, Andrew King, Olivier Caty, Sébastien Denneulin, Éric Martin

Quantitative thermomechanical characterisation of 3D-woven SiC/SiC composites from in-situ tomographic and thermographic imaging.

Léonard Turpin[a,b,c,*], Stéphane Roux[b], Jean Bénézech[a,c], Guillaume Couégnat[a], Andrew King[d], Olivier Caty[a], Sébastien Denneulin[c], Éric Martin[a]

[a] *CNRS/CEA/SAFRAN/Univ. de Bordeaux, LCTS - Laboratoire des Composites Thermo-Structuraux, F-33600, Pessac, FRANCE*
[b] *Univ. Paris-Saclay/CentraleSupélec/ENS Paris-Saclay/CNRS, LMPS - Laboratoire de Mécanique Paris-Saclay, F-91190, Gif-sur-Yvette, FRANCE*
[c] *Safran Ceramics, F-33700, Mérignac, FRANCE*
[d] *Synchrotron SOLEIL, F-91192, St-Aubin, FRANCE*

Abstract

3D woven composites are often modelled using homogenisation whose foundation requires the validity of *scale separation* — microstructure scale much smaller than any other scales from part geometry, manufacture or loading — often violated in reality. Modelling has then to be confronted with experimental data representative of actual service conditions. A high-temperature multiaxial thermomechanical test is carried out on an L-shaped specimen. It is followed by synchrotron X-ray tomography and infrared thermography. The coupling of the complex geometry and weaving pattern, and a non-homogeneous thermal field, induces a very irregular stress field inside the sample, generating locally unusual loading configurations. Integrated digital volume correlation provides a fine identification of the material parameters of an image-based mesoscale model. Most involved parameters are identified with good precision, including tow shear moduli. The model is able to describe the sample deformation in the elastic domain accurately.

*Corresponding author
Email address: leonard.turpin@ens-paris-saclay.fr (Léonard Turpin)

Keywords: Ceramic-matrix composites (CMCs), CT analysis, mechanical testing, thermomechanical

1. Introduction

To reduce the impact of air traffic on the environment, aircraft manufacturers aim to enhance engine efficiency by increasing the service temperature in the combustion chamber. This upgrade requires materials sustaining high thermomechanical performances up to 1500°C [1]. 3D-woven SiC/SiC ceramic matrix composites (CMCs) are very promising as they exhibit excellent structural properties at high temperatures [2]. The woven structure makes those materials resistant to impact and delamination [3]. For aeronautical parts with intricate geometry, complex woven structures are designed to resist multiaxial non-homogeneous loadings [4]. A thorough understanding of thermomechanical behaviour, especially for critical areas, is required to design, model and certify such parts [5].

Recent studies bring out the determining influence of the micro- and mesostructure of SiC/SiC CMCs on their local or overall behaviour [6, 7]. Numerous works propose suitable micro-to-meso homogenisation [8, 9], and microstructure influence is well understood for regular geometries, typically coupon samples or weaving patterns [10]. Image-based models can reproduce the behaviour of materials presenting complex microstructure [11, 12], and homogenisation procedures have been developed [13]. Stochastic generation of elementary cells representative of the fibre distribution inside the tows allows taking into account the heterogeneity at the micro-scale [14]. Nevertheless, for meso-to-macro homogenisation, defining a representative volume element is not always possible. Indeed, most actual parts have complex shapes (e.g. aeronautical parts such as turbine blades or containment rings) [15]. In such parts, the CMC displays large microstructure changes (e.g. bending with high curvature, changes in weaving patterns) — the fabric can even be non-periodic. Moreover, the characteristic lengths of the loading (e.g. $T/\|\boldsymbol{\nabla} T\|$ for thermal gradient, $1/\|\boldsymbol{\nabla}\varepsilon\|$ for strain),

which are closely linked to the geometry, can also become smaller than the *putative* representative volume element length. Theoretically, usual homogenisation approaches reach their limits. The mesostructure is critical, and its influence is not properly characterised yet. The lack of experimental procedures to assess the representativity of image-based models is one of the main impediments to their further deployment for industrial uses. This study aims to validate (or invalidate) the use of homogenisation procedures out of their secured field of application. It is then crucial to confront the model and the experiment.

An experimental procedure has been developed to characterise complex-shaped samples. To challenge current model hypotheses, geometry needs to be 3D, and the thermomechanical loadings have to be heterogeneous. Such tests require innovative instrumentation. X-ray tomography is a tool capable of accessing the material mesostructure [16]. It provides a 3D image of the X-ray absorption coefficient. Local damage due to loading can be observed and measured by conducting *in-situ* experiments instrumented by tomography [17]. This technique is especially efficient in observing cracking (localisation, morphology, etc.), provided the crack opening is greater than the voxel scale. Tensile tests have already shown the capability of such an approach for the study of CMCs at high temperatures [18, 19]. During in-situ tests, X-ray tomography coupled with Digital Volume Correlation (DVC) gives access to the displacement field in the bulk of the sample [20, 21, 22]. From either measured strains or DVC residuals, cracks can be detected even with subvoxel openings. The displacement field is computed relying on the texture of the volume, which is nothing but the mesostructure of the woven sample. This mesostructure limits the accuracy and resolution of the DVC-computed displacement field [23]. A relevant way to bypass this limitation is to take into account the sample model during DVC computation performing *integrated*-DVC (IDVC) [24]. For thermomechanical experiments, infrared thermography can provide the surface temperature field to be used as thermal boundary conditions for IDVC [25].

The present paper details the identification of mesoscale material parameters of an image-based model that conforms to the actual mesostructure using

in-situ experiments. The purpose is to understand better the behaviour of genuine CMC parts under complex loading. Experiments were carried out on a dedicated thermomechanical testing machine, described in [4], on the PSICHE beamline at synchrotron SOLEIL. The sample was subjected to severe thermal gradients and multiaxial loadings. Based on a self-calibrated projection model, infrared images are cast on the sample 3D finite-element mesh surfaces [26]. The high load capacity of the testing machine required the presence of stiff columns that partly obscured the projections (radiographs). Nevertheless, using a tailored reconstruction procedure and artefact corrections, one could successfully reconstruct high-quality 3D images [27]. The present study exploits such images.

Exploiting the considerable amount of data provided by full-field measurements is quite challenging. An original IDVC procedure was therefore developed to identify parameters of a model enabling, in turn, its validation.

The procedure is described in section 2: the construction of the model is detailed, together with the identification method. Section 3 presents the identification results of a high-temperature test on an L-shaped sample. In section 4, the quality of the results and the relevance of the chosen model are discussed. Concluding remarks and perspectives are proposed in section 5.

2. IDVC procedure

2.1. In-situ experiment

The test is an in-situ *corner bending test*, described in detail in a companion paper [4]. The sample is an L-shaped corner. Its inner radius is 4 mm. The long arm is 27 mm, the short one 12 mm, with a section of $4.15 \times 3\,\mathrm{mm}^2$ (Fig. 1a). The long arm is clamped during the experiment. First, a thermal loading is applied by heating the outer surface of the long arm (using a resistor) to generate a high temperature gradient in the zone of interest (Fig. 1b and 1c). Once the sample reaches the prescribed temperature, a mechanical load is applied incrementally in the $-z$-direction, up to rupture, by an alumina punch on the short arm (Fig. 1b).

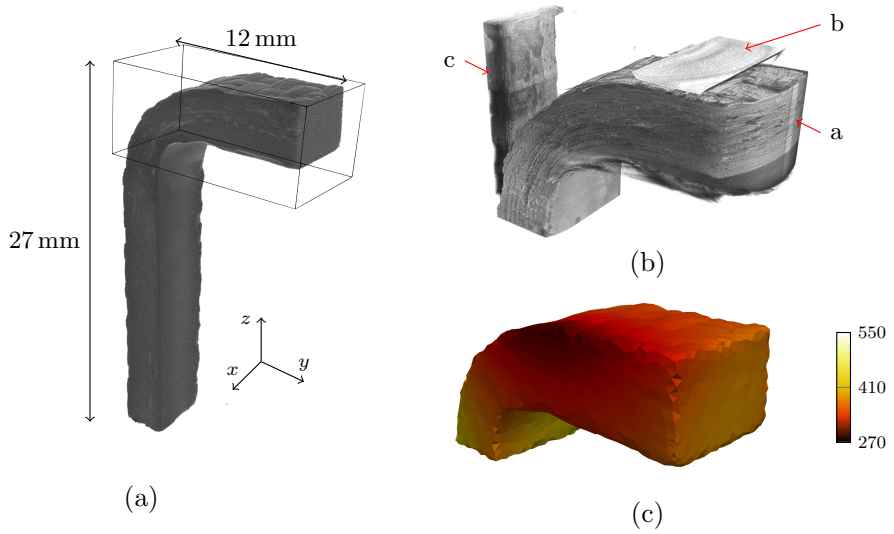

Figure 1: L-shaped sample. (a) Tomography of the full sample. (b) Zone of the sample visible during the test (the short arm **a**); the mechanical loading is applied by the punch **b**, the thermal loading is applied by the SiC/SiC resistor **c**. (c) Thermal field at the first loading step (°C)

An infrared camera is set up such that its optical axis is perpendicular to the tomograph X-ray axis. A set of thermographies is acquired during the tomographic scan while the sample is rotating, giving access to the thermal field of all the sample surfaces. The tests are carried out on the PSCHE beamline at synchrotron SOLEIL with a pink beam centred around 40 keV and at a resolution of 3.14 µm. Those acquisition conditions provide a sufficient texture for DVC (i.e. grey-level variations in the tomographic images), a good description of the mesostructure of the sample and a large enough field of view to observe the whole zone of interest. The resolution of infrared images is 217 µm. For more details about the acquisition conditions, the reader is referred to [4].

Tomographic and thermographic acquisitions are performed at the initial state at room temperature, after the heating step and at each loading step.

2.2. Thermomechanical model

The structure of woven-SiC/SiC composites is complex (Fig. 2). The studied material is produced by Safran Ceramics. At the mesoscale, two constituents are generally distinguished [4]:

- the tow, composed of Hi-Nicalon-S SiC fibres, coated by a boron nitride interphase and the intra-tow SiC matrix, both elaborated by Chemical Vapor Infiltration [18];
- the SiC matrix which is elaborated in two steps (SiC slurry cast and metal Si Melt Infiltration (MI) [28]) and thereby contains several phases (SiC, Si and SiC powder embedded in metal Si) and has an overall porosity of about 5% [4].

Those phases are considered homogeneous, the identified mesoscale properties are thereby effective properties which will depend on the microstructure. The mesopores are explicitly considered on the model because their repartition is not homogeneous in the material, at least at the considered imaging scale. The micro-cracks and porosity are assumed to be more diffuse and integrated into the matrix effective mesoscale properties. Moreover, their very small size and aperture prevent their observation. They are thus not considered explicitly, but from their contribution to the effective elastic properties of the matrix phase. The woven pattern, a custom 3D interlock, has a prominent influence on the thermomechanical behaviour of the composite. The *image-based model* deployed in the following aims to reproduce this effect.

As described in Appendix A, a sample woven structure is characterised explicitly by textile descriptors: neutral fibres of tows and several sections having a polygonal geometry. A descriptive geometrical model of the preform can then be built. The present study chose to resort to an idealised description of the weaving based on a simulation of the preform shaping process. The matrix geometry (overall sample shape and mesoscale pore distribution) is extracted from the tomography and integrated into the model. The simulated weaving does not match the actual mesostructure perfectly. Nevertheless, the possibility

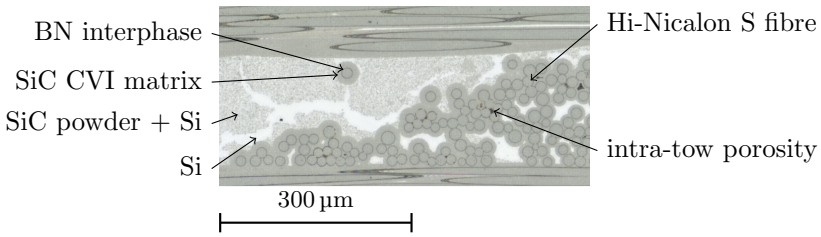

Figure 2: Microstructure of the studied SiC/SiC composite (courtesy of V. Mazars, this image is reproduced from [6]).

of using a simulated model instead of the actual sample microstructure is an attractive supplementary feature of the proposed methodology. The validation of the preform shaping simulation is also an important issue, although it is not addressed in the present paper.

The composite elementary constituents are assumed to have a linear thermoelastic behaviour in the ranges of temperature and strain applied. The matrix is isotropic, and the tows are transversely isotropic. They are both considered homogeneous, and the properties of all tows are chosen identical. Table 1 inventories the whole set of the constituent material properties and the notations used hereafter. As the thermal gradient in the sample is important, the variation of the properties with temperature has to be considered. In the considered temperature range (room temperature up to 1200°C), the SiC properties vary linearly [29]. This observation is extended to the properties of tows. Properties are then considered at the two bound temperatures. As the anisotropy of the expansion coefficient of tows is low and its value is close to the matrix one, it is considered that the expansion coefficients of the tows are equal to that of the matrix $k_{11} = k_{22} = k$. Indeed, the two expansion coefficients of the tows, k_{11} and k_{22}, have very low sensitivities and induce ill-conditioning of the identification problem, as explained in Appendix C. Therefore, 18 mesoscale material parameters in total need to be identified.

The used macroscale mesh does not describe the mesostructure explicitly (Fig. 3a). A local homogenisation is required. The effective properties of each

	description	T (°C)	initial	estimated	uncertainty
E (GPa)	matrix Young's modulus	20	310	304	2
		1200	276	202	5
ν	matrix Poisson's ratio	20	0.17	0.17	1×10^{-4}
		1200	0.17	0.17	6×10^{-5}
k (K^{-1})	matrix coefficient of	20	4.7×10^{-6}	4.16×10^{-6}	1×10^{-8}
	thermal expansion	1200	9×10^{-6}	8.74×10^{-6}	3×10^{-8}
E_{11} (GPa)	tow longitudinal Young's	20	320	320	3
	modulus	1200	306	303	5
E_{22} (GPa)	tow transverse Young's	20	146	127	2
	modulus	1200	120	122	2
G_{12} (GPa)	tow shear modulus	20	59.6	60	5
		1200	47.6	54	6
G_{23} (GPa)	tow shear modulus	20	64.8†	47	2
		1200	64.8†	44	4
ν_{12}	tow Poisson's ratio	20	0.176	0.17	3×10^{-2}
		1200	0.175	0.17	3×10^{-2}
ν_{23}	tow Poisson's ratio	20	0.15	0.12	4×10^{-2}
		1200	0.137	0.12	4×10^{-2}

Table 1: Thermomechanical properties of the meso-constituents. Initial values are from [30] and †[15]. The identified values are the IDVC result. Comments on the computation and the meaning of the displayed uncertainties can be found in Appendix D

element are computed from the properties of the constituents it contains using an equivalent laminate model using the procedure detailed in Appendix A. It results in a field of stiffness and thermal dilatation tensors different to each other. The number of macroscale parameters is huge, but for a given geometry, they depend on a limited number of mesoscale parameters.

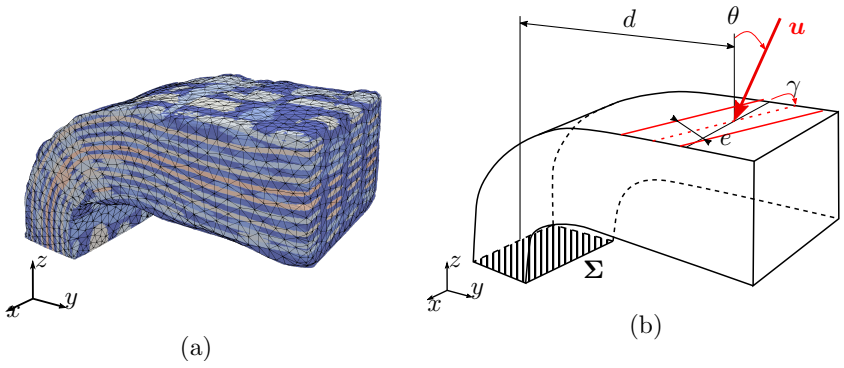

Figure 3: Model of the sample. (a) Mesostructure and the macroscale mesh (mesh size 252 µm), the colours refer to the elementary constituents. (b) Boundary conditions, the bottom surface $\mathbf{\Sigma}$ is not a free surface, and its rigid body motion and dilatation are computed from DVC. The loading applied by the punch is displayed in red and parameterised by $\{u, d, e, \theta, \gamma\}$

The sample is clamped in its lower part. In the model, the bottom surface of the mesh, $\mathbf{\Sigma}$, is assumed to be subjected only to rigid-body displacement and thermal dilatation (Fig. 1c). Those parameters are determined by standard DVC over a zone of interest surrounding this surface. The loading is applied to the short arm with a punch. The punch geometry was chosen to be flat, and it is assumed that the entire lower surface of the punch is in contact with the sample. The temperature field is re-projected from multi-view infrared acquisition (Fig. 1c). It was shown to remain constant in time during an acquisition [4], and it is used as Dirichlet thermal boundary conditions applied to the model surface.

2.3. Identification procedure

The experimental protocol aims to identify the best meso-constituent material parameters of the image-based model (listed in Table 1) to fit the observed behaviour. It is then used to validate the modelling choice.

DVC consists in computing the displacement field between two tomographic images based on their texture and assuming grey level conservation [22]. With global DVC, the displacement field is expressed on a kinematic basis, itself supported by a finite element mesh. The exploited image texture of the tomographic reconstruction is directly the contrast of the microstructure without any further alteration. In the considered composites, the tows are not uniformly distributed, and the major axes of the tow sections have lengths of the same order of magnitude as the thickness of the part. In classical DVC, the mesh should be very coarse. A more tailored basis can be used. IDVC directly uses a kinematic basis composed of the sensitivity fields with respect to the parameters of the sample model [31]. Among full-field measurement-based methods, IDVC is the best identification procedure to minimise the uncertainty of the identified parameters, provided the model accurately describes the sample and its boundary conditions [24].

Appendix B details the IDVC procedure and its implementation in our particular case. In essence, IDVC aims to find the set of parameters that minimises the norm of this DVC residual (i.e. the difference between the reference image and the deformed image corrected by the current estimation of the displacement field). A Gauss-Newton algorithm is used. The residual is projected onto the vector space generated by the sensitivity fields of the parameters. The respective amplitude of those projections provides the estimate of the incremental correction of the parameters. The convergence criterion is defined using the norm of this incremental correction, ensuring the stationarity of the solution. As long as the material can be considered linear thermo-elastic, its properties do not vary from one acquisition step to another. It is, therefore, relevant to perform only one minimisation embracing all the steps in a so-called spatiotemporal approach.

3. Results

3.1. Model validation

This approach is valid as long as the thermo-elastic model remains relevant. Therefore, our analysis is performed over all data collected prior to the first visible sign of damage. The measured temperature and displacement fields of the elastic step of the test are displayed in Figure 4. The temperature fields are directly a projection of the infra-red images onto the sample mesh. The "measured" displacement fields are computed with the model using the identified set of parameters. Only thermal loading is applied during the first step (a), and the sample expands. As the thermal loading does not evolve much during the test, the displacement field at this step gives an insight of the thermal-induced displacement all along the test. The mechanical loading is applied during the following steps (b) to (d), and the sample bends about the x-axis. The amplitude of the thermal-expansion-induced displacement is relatively important compared to the mechanical one. On the thermal field, the effect of the contact with the punch, acting as a heat sink, explained the temperature variation between steps (a) and (b).

The identification procedure is initialised with material properties extracted from the literature (Table 1). The displacement field determined by the first finite element simulation provides the initial residual. If the model perfectly reproduces the measured displacement field, those residuals should reduce to noise images. The image textures should not be detectable. In practice, identification procedures, such as IDVC, reduce the kinematic basis drastically. The new parametric basis limits the solution to relevant ones.

Figure 5a corresponds to the heating step (without any mechanical loading), and Figure 6a to the first mechanical loading step (resp. step (a) and (b) of Figure 4). The remaining texture on the residual field traduces the local error on the simulated displacement field. The grey level amplitude is irrelevant per se, but the patterns provide the mismatches between the model and the experiment. In Figure 6, a porosity is marked with an arrow in the (x, y)-plane. It displays

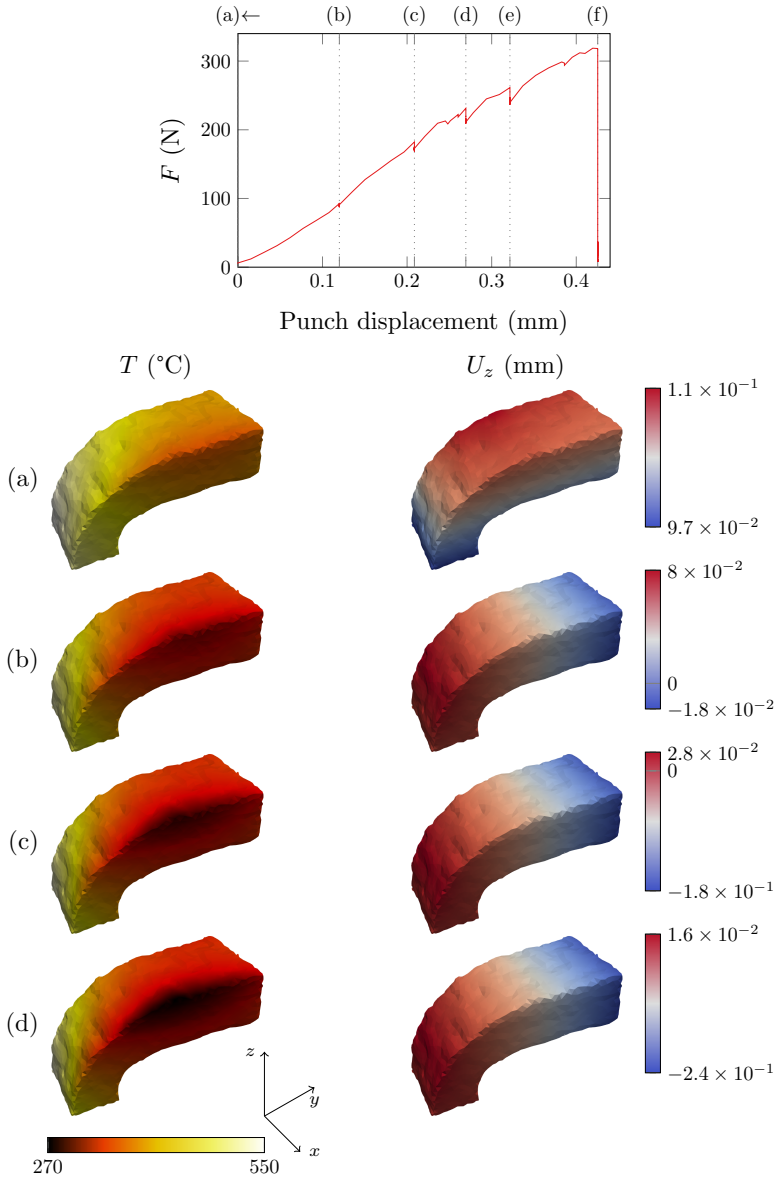

Figure 4: High-temperature corner bending test. In the force/displacement curve, the acquisition steps are marked by letters (a is the heating step; b, c, d, e and f are the mechanical loading steps). The temperature field and z-component of the displacement field are issued from the FE simulation with identified material parameters. Only elastic steps are considered here.

two lunulae, one positive and one negative, meaning the recalled position of this porosity is false. A displacement along y is missing.

However, the overall displacement is rather well determined with the initial parameters. The chosen model and properties are suitable as they already account well for the kinematics from the tomographic data. The identification procedure aims to fine-tune the material properties to minimise these residual fields further.

The norm of the residual (i.e. the root mean square of the residual field) provides global information about the mismatch between the two images. Its variation is a good indicator for comparing several models and parameters. The residual norm with the identified set of parameters should be lower than the initial one.

3.2. Identification of the material parameters

Table 1 gathers the results of the identification of thermo-elastic material properties for a high-temperature test. In general, the differences between optimised and initial values are relatively low. However, substantial differences have to be noticed.

The initial choice of the matrix Young's modulus was overestimated, whereas the thermal expansion coefficient was underestimated. Considering the matrix as homogeneous at the mesoscale is daring, given its actual heterogeneity. Indeed, due to the woven-structure shaping, some regions between and inside tows are difficult to infiltrate and present shrinkage cracks and micro-pores. Although the resolution of the tomography is not sufficient to observe them, such cracks are expected within the slurry cast sintered matrix [32]. IDVC, by identifying the effective mesoscale properties, allows for taking into account the softening of the matrix induced by the micro-porosity and micro-cracks. Furthermore, the estimation of the mesoscale porosity is imperfect. As an ideal woven structure is used to build the model, which is not a perfect match to the real structure in places, the porosity map obtained from tomography intersects some tows. So as not to break their continuity, those pores are omitted, thereby reducing the

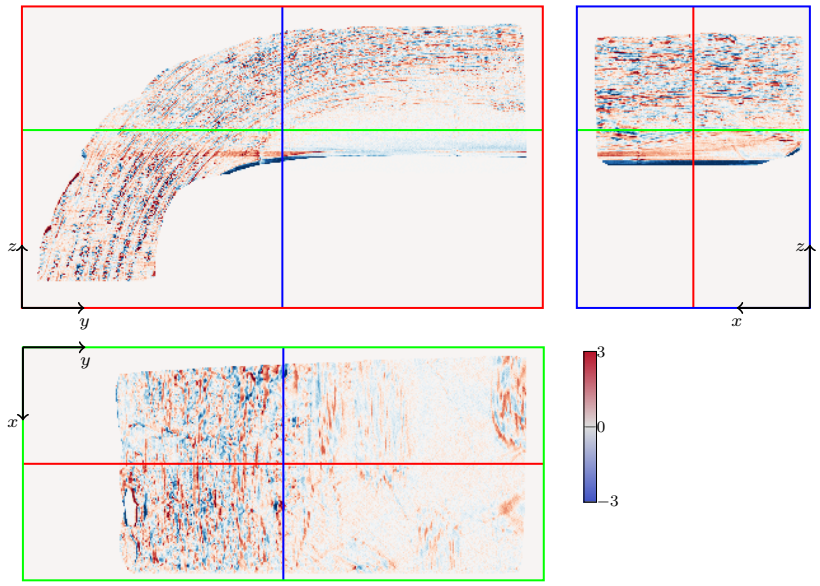

(a)

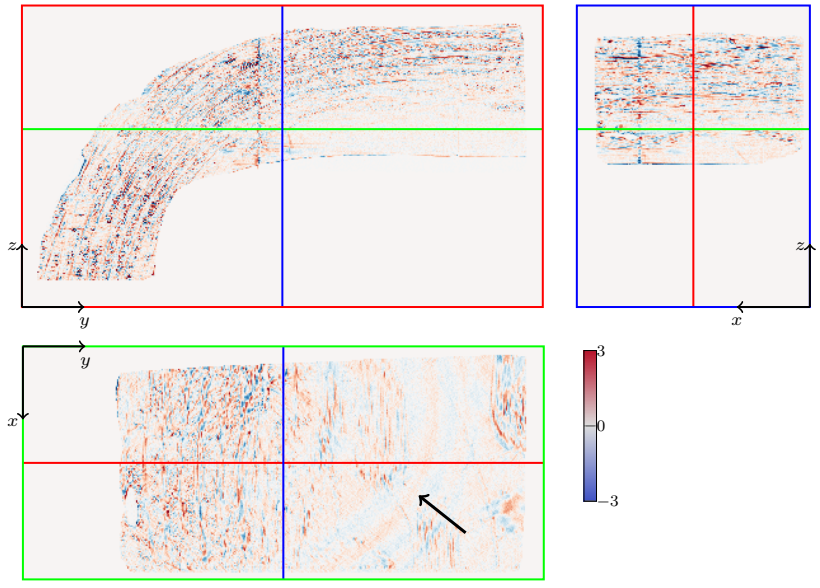

(b)

Figure 5: Grey level residual field, ρ, for the heating step: (a) initial state $\|\rho\| = 5.54 \times 10^3$; (b) converged state $\|\rho\| = 4.28 \times 10^3$. Some ring artefacts are pointed out by the arrow in the (x, y)-plane at the converged state.

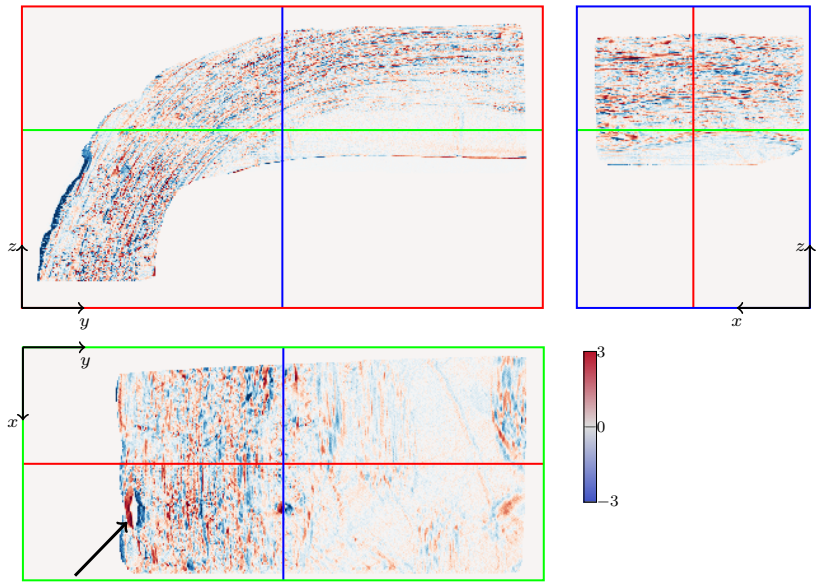

(a)

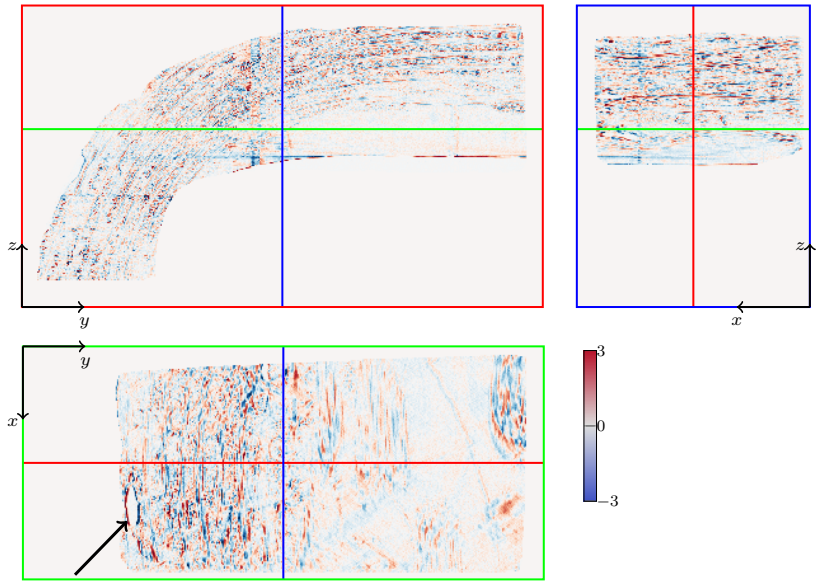

(b)

Figure 6: Grey level residual field, ρ, for the first loading step: (a) initial state $\|\rho\| = 5.66 \times 10^3$; (b) converged state $\|\rho\| = 4.95 \times 10^3$. In (x, y)-planes, arrows mark the position of a mismatching pore.

actual porosity of the sample. The insufficient knowledge of the micro-structure of the matrix could explain the initial overestimation of Young's modulus E. The rather large correction of high-temperature E can result from the presence of the metallic Si phase. The properties of this metallic phase vary much more with the temperature than those of the SiC ceramic phase.

The initial values of tow properties are the effective parameters proposed in [30], which stem from homogenising unidirectional tows. Only the fibre, the interphase and the intra-tow matrix are considered during the homogenisation. Regarding the longitudinal properties of tows, the final values remain close to the initial ones. The fibres dominate the longitudinal properties. They are thus less sensitive to microporosity. The elementary homogenisation to determine them is efficient. Although homogenisation is rather coarse, the results appear to be accurate despite the high tow curvature in the elbow of the sample. For the transverse properties, particularly the shear modulus G_{23}, identified values are significantly lower than their initialisation. Micro-mechanical simulations of tows show that their porosity substantially impacts their transverse properties [33]. The underestimation of porosity and intra-tow matrix discontinuity could be responsible for the initial overestimation of the transverse properties. As pointed out in [4], the infiltration of our samples is not perfect, and the tow porosity may be a little higher in bulk than near the specimen surface.

4. Discussion

A complex test, such as the presented corner bending test, is an excellent way to access a large set of material properties. As the loading state of the sample varies from one area to the next, most constitutive parameters influence the observed displacement fields. This loading heterogeneity should be contrasted with standard approaches where each property is evaluated with a dedicated test. Not only does the proposed procedure reduce the time and effort of a complete experimental campaign, but it also avoids sample variability, which may affect the interpretation.

The influence of each parameter can be evaluated by considering the diagonal terms of the Hessian matrix of the sensitivity matrix (Appendix D). The good conditioning of the Hessian matrix allows one to judge the relevance of the considered test to identify the sought parameters. Indeed, the conditioning quantifies the relative influences of the least and the most sensitive combinations of parameters.

The errors remaining after the identification are measured by the final residual. Two types of errors can be distinguished:

- the model error;
- the measurement uncertainty.

4.1. Model validation: considerations about model error

The model error is the gap between the actual sample behaviour and its simulated behaviour. It induces an error in the converged displacement estimation, which appears distinctly in residual fields. In the present case, the model error can be explained for the most part by the use of an ideal woven structure to build the enriched macro-scale model of the sample instead of the actual one. The homogenisation hypotheses are a potential source of error. As evoked in Section 3.2, considering the matrix as a homogeneous media at the mesoscale is a strong assumption. Similarly, assuming that all tows have the same properties is an approximation.

Tomographic artefacts are an additional source of model error. Indeed, volumes with artefacts do not faithfully reproduce the sample microstructure and can affect DVC computation. Performing DVC, the grey levels of the image are thus expected to be an intrinsic signature (X-ray absorption coefficient) of each sample voxel. The grey level of a material point is assumed not to vary during the test. However, scattering may induce deviation from such assumptions. Most tomographic artefacts, namely missing-angle and ring artefacts, are static in the detector frame and do not move as neighbouring material points from one step to the next. It is essential to reduce these artefacts by pre-processing the volumes [4, 27]. As they do not entirely vanish, some remain visible in

the residual. For instance, some ring artefacts are visible in Figure 5b in the (x, y)-plane.

Figure 5 shows the residual of the heating step at the beginning of the test. The model adequately reproduces the displacement field induced by the thermal expansion as the residual almost exclusively reveals noise and tomographic artefacts.

Figure 6 corresponds to the first loading step. Even though the displacement field is globally well estimated (the model captures the sample boundary motion well), the woven structure appears in the residual. The model with identified parameters does not perfectly describe the local deformation of the sample. Nonetheless, the deviations from experimental data are low. The mismatch on the sample edges can be measured to estimate the error in displacement using the model with identified parameters. The good agreement between the model and the experiment in this case, with high thermal gradients and important microstructure variations, validates the relevance of using local homogenisation.

A way to improve the finite-element model could be to take into account the true mesostructure, obtaining textile descriptors from the tomography of the sample. In SiC/SiC composites, the contrast between matrix and fibres is poor because both are made of silicon carbide. The segmentation of the woven structure is thus difficult on fully elaborated materials. Bénézech and Couégnat [34] proposed to perform this step before the infiltration of the matrix (on the so-called *woven preform*). Unfortunately, in the present experiment, the woven preform tomogram was unavailable.

4.2. Influence of parameters: considerations about uncertainties

The measurement uncertainty is induced by the noise on the raw measured fields, i.e. the noise level of the tomograms and the uncertainty of the force. The noise of the tomograms is assumed to be white and Gaussian. It is estimated as the variance of grey levels in a homogeneous area of the tomogram (in the air surrounding the sample). The measurement uncertainty of the force is computed from the manufacturer's data about the acquisition chain (force sensor

and acquisition device). The uncertainties displayed in Table 1 are computed from the uncertainty of the experimental data as explained in Appendix D. It corresponds to the uncertainty on the parameter if there were no model errors and if all other parameters were set to their values. It is a lower bound of uncertainties. To fully characterise the uncertainty, it is necessary to consider the coupling between parameters and the full covariance matrix of the problem (or its invariants, e.g. its eigenvalues).

Considering a sub-problem with two degrees of freedom, Figure 7 illustrates the coupling of parameters for two pairs of parameters: (a) room-temperature E and E_{11} (matrix and tow Young's moduli, respectively) and (b) room-temperature G_{12} and G_{23} (tow shear moduli). For the latter, the ellipse axes are almost parallel to the basis axes, G_{12} and G_{23} are only slightly correlated. Hence, the previous conservative estimates do coincide with the true uncertainty. In contrast, the two parameters are very much correlated for the former. The estimation of the uncertainty should take into account the coupling.

For the full problem, the uncertainty hyper-surface is a 22-dimension hyper-ellipsoid whose full knowledge is necessary to assess the uncertainty of any property which depends on any arbitrary combination of parameters. From an engineering point of view, such a determination is impractical and difficult to communicate. In practice, one generally aims to determine one parameter considering all others as known. The uncertainty on that parameter is then the intersection of the ellipsoid with the line describing the quantity of interest.

In a given experimental condition, with a given amount of data, the smaller the number of identified parameters, the lower the uncertainty. With that in mind, the proposed spatiotemporal approach is relevant. The material is assumed linear elastic. The material parameters are thus independent of the loading level and can be determined once for the entire test. The overall number of parameters to be identified is so substantially reduced.

The uncertainty obviously depends on the sensitivity of the displacement field on the corresponding parameter. It traduces the capability of the IDVC procedure to identify a particular parameter. Here, relative uncertainties vary

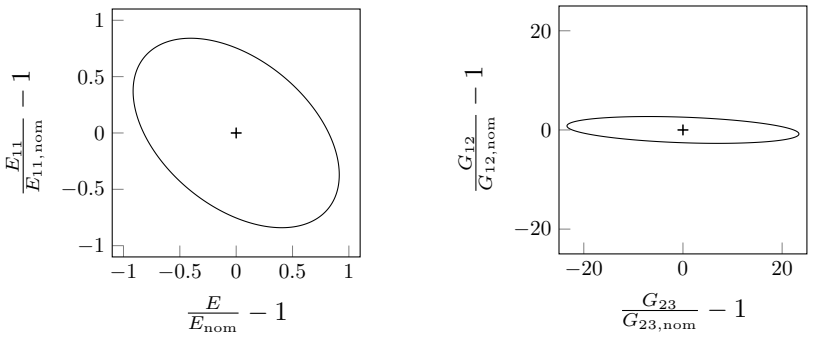

(a) with RT E and E_{11} (b) with RT G_{23} and G_{12}

Figure 7: Uncertainty ellipses (%) for some two-parameter problems. Each parameter is normalised by a nominal value, typically its initial guess.

from 0.24% for room temperature expansion coefficient (k) to 33% for the tow ν_{23} Poisson's ratio. Such a large uncertainty means that the Poisson's ratio has basically no influence on the kinematics. Even a rough approximation of this parameter provides a good description of the sample behaviour. This is an additional motivation for carrying out a test representative of operating conditions, whatever their complexity.

Here the temperature field is treated as exact, and thus the error in the temperature measurement is not included in the uncertainty but the model error.

4.3. Limitation of the IDVC algorithm

Such an approach is demanding in terms of computation time. The convergence is slow. The IDVC itself requires about two hours for the high-temperature test. The limiting step is the determination of sensitivity fields, which necessitates as many finite-element simulations as parameters to identify. So increasing the number of parameters of the model implies higher computation times. A relatively complex thermo-elastic model is used here, and each simulation takes about one minute. Using a more complex model, e.g. including damage, could require high-performance computation setups.

5. Conclusion

This work opens the way to fully characterise industrial parts rather than samples of material lacking shape complexity. The proposed IDVC procedure, based on a locally homogenised model, is applied to a sample that does not fulfil the scale separation hypothesis. IDVC provides model validation, fine identification of material parameters and uncertainty estimations. A corner bending test proves to be well-suited to identify most of the thermo-elastic parameters of the model.

The identification residuals highlight a good agreement between the proposed model and experiment, proving the capability of a macroscale locally-homogenised model to accurately describe the thermomechanical behaviour of SiC/SiC CMCs up to damage occurrence and despite the complex shape of the sample. The deformation of a 10 mm-long sample is reproduced with a precision of about 20 µm.

A set of nine material parameters is identified. Considering the gap between the initial guess and the estimated parameters, the quality of usual hypotheses about elementary properties, which is generally the weak point of homogenised models, can be assessed. Most of the identified parameters are close to the initial ones. It means, for instance, that a common homogenisation to compute tow properties already provides a good approximation of effective behaviour even if those tows present a large curvature. Nonetheless, the tow transverse properties were initially overestimated. This is likely due to neglecting intra-tow micropores. The sensitivity fields highlight the influence of the identified parameters in the given loading configuration. As expected, the matrix properties have a first-order influence on the behaviour in the elastic domain, and so do the longitudinal and transverse tow Young's moduli. On the other hand, the tow Poisson's ratios appear to have a weak effect.

The part geometry renders its manufacturing delicate. For instance, the fibre volume fraction or Si fraction in the matrix may differ from the one expected during the initial design. The identified parameters provide — for the

studied sample and the considered model — the best description of the sample behaviour. The model needs to be validated by further experimental studies for design or certification purposes. This procedure — or a similar one — should be extended to other test configurations to fully validate the modelling choices (varying loading, geometry and weaving of the sample). Then, the model and the identified material parameters could be used to design and dimension parts.

Acknowledgement

It is a pleasure to acknowledge Capucine Billard, Hugo Carpentier, David Damiani and André Ebel for their help during experiments and Xuyang Chang for his critical reviewing.

This work was supported by *Association Nationale de la Recherche et de la Technologie* and Safran Ceramics (CIFRE grant); Safran group and *Direction Générale de l'Aviation Civile* (PRC MECACOMP); and synchrotron SOLEIL, St-Aubin, France (proposal 20181639).

Appendices

A. Image-based model and homogenisation procedure

The objectives are, on the one hand, to build a model taking the sample mesostructure into account and, on the other hand, to keep some freedom in terms of element sizes. A macroscale model is *enriched* by computing the material properties from the mesoscale constituent properties using a local homogenisation procedure.

A simulation of the forming of the weaving pattern provides the sample tow geometry as textile descriptors (neutral fibres and sections of the tows, using the formalism proposed by [34]), displayed in Figures A1a and A1b. Thanks to those descriptors, each tow and each tow segment are labelled. Two volume images are built using those labels as grey levels (Fig. A1c). The images represent the geometry of the weaving pattern. The labels are resp. related to a table of phases and a table of orientations.

The overall infiltrated sample shape is determined thanks to the tomography, and so is the mesopores distribution [4]. Tomography provides the geometry of the matrix as a binarised image (Fig. A1d). A new image is built by summing the weaving pattern and the matrix images (Fig. A1e). It represents the spatial distribution of the different phases. The mesopores are considered in the model only when they do not intersect the idealised woven structure. From this image, a mesoscale mesh is formed using the CGal toolbox [35]. The mesh contains 345 000 nodes and is composed of tetrahedral elements.

At the mesoscale, tows are assumed to be transverse-isotropic and homogeneous. The matrix is supposed to be isotropic and homogeneous. The interfaces between tows and matrix are assumed to be perfect (no de-cohesion is considered). The interface nodes are shared by the two surrounding phases ensuring the displacement continuity between the phases. The pores are considered isotropic with a very low Young's modulus. The mesoscale properties are recalled in Table 1.

The macroscale mesh is also built using CGal, using the binarised tomogram

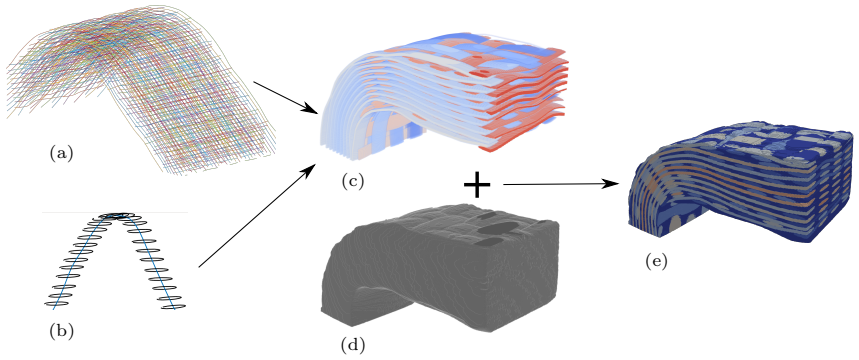

Figure A1: Building of the mesoscale image-based model. The textile descriptors of the fabric (a) and of the geometry of the tows (b) are used to build 3D images of the weaving pattern (c). A binarised tomography (d) gives the overall shape of the sample and so the geometry of the matrix. Addition of those two images, image (e) describes the spatial distribution of the mesoscale components.

of the sample. It contains 4560 nodes. It faithfully reproduces the overall geometry of the sample and is, by construction, in the same frame as the mesoscale model. Macro-elements contain more than one phase (Fig. A2a, A2b and A2c). The effective properties of each macro-element are computed from the properties of the phases it contains using an equivalent laminate model. The macro-element effective stiffness tensor, $\mathbb{C}_{\text{eff}}$, and thermal expansion tensor, $\mathbb{K}_{\text{eff}}$, are then the weighted means of the resp. tensors of each phase i (all the tensors expressed in the global frame)

$$\mathbb{C}_{\text{eff}} = \tau_i \mathbb{C}_{\text{i}} \qquad \mathbb{K}_{\text{eff}} = \tau_i \mathbb{K}_{\text{i}} \tag{A1}$$

In practice, those properties are computed from tables containing the proportion, τ_i, and orientation of each constituent of the macro-element using a dedicated Abaqus UMAT (*User-defined mechanical MATerial behaviour*) [15]. This UMAT also takes into account temperature dependence. Properties are assumed to vary linearly with the temperature in the considered range. Each macro-element has thus different properties. As an illustration, Figure A2d

shows the fields of some components of $\mathbb{C}_{\text{eff}}$. One can notice that the tow alignments appear on the field along their transverse direction. Mesostructure data is transported into the macroscale model.

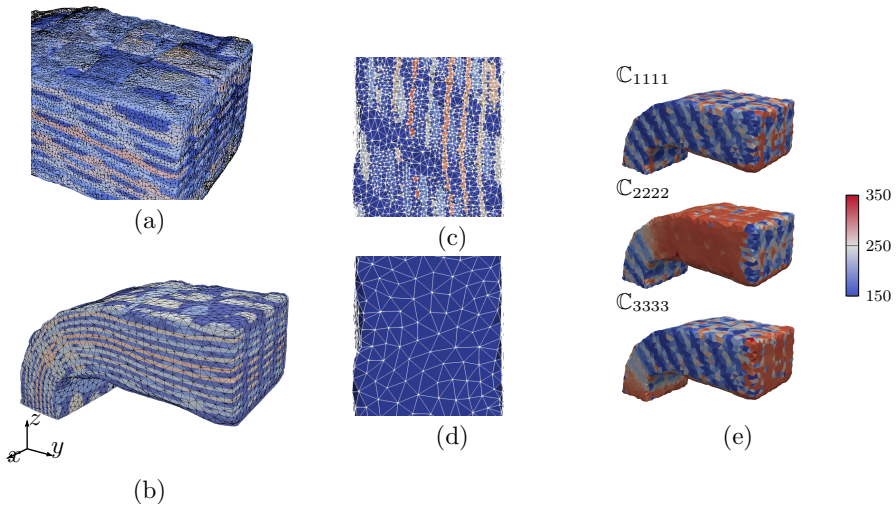

Figure A2: Local meso-to-macro homogenisation. (a) Zoom on the mesoscale mesh, superimposed with the image of the weaving pattern; (b) Macroscale mesh superimposed with the image of the mesostructure. The mesoscale mesh (c), with a mesh size of 90 µm, is conformal, whereas the macroscale mesh (d), with a mesh size of 225 µm, is not. (e) Fields of the three first diagonal components of the macroscopic effective stiffness tensor $\mathbb{C}_{\text{eff}}$ (GPa) issued from the local homogenisation.

The macroscopic mesh size is a compromise between modelling and DVC constraints. On the one hand, tomography texture imposes the minimal element size for DVC. On the other, too large a size downgrades the quality of the local homogenisation. Indeed, the hypothesis of the local equivalent-laminar model is relevant only if the element contains, at most, one weft and one warp tows. The tows have an ellipse shape with a major axis of about 600 µm and a minor axis of about 200 µm. On a comparable SiC/SiC composite, a mesh size of 252 µm, thus corresponding to the yarn thickness, is sufficient to bring to light the effect of mesostructure heterogeneity on the elastic behaviour properly [15]. This size is used to build the macroscale model. This last model has 13 680 degrees of

freedom.

B. IDVC implementation

DVC is an imaging technique which aims to compute kinematic fields from volume images (typically tomograms) acquired at different loading states [31]. It consists in finding the displacement field, $\boldsymbol{u}$, minimising the residual, ρ, between two images, f and g

$$\rho\left(\boldsymbol{x},\boldsymbol{u}\right)=f\left(\boldsymbol{x}\right)-g\left(\boldsymbol{x}+\boldsymbol{u}\left(\boldsymbol{x}\right)\right) \tag{B1}$$

In the global formulation, the weak form of the problem is considered. The displacement field is projected on a finite element basis $\boldsymbol{u}(\boldsymbol{x}) = a_i\varphi_i(\boldsymbol{x})$ [36]. The problem is highly non-linear. It is solved using a Gauss-Newton algorithm. The iterative correction, $\{\delta a\}$ of the displacement field $\{a\}$ is found by solving

$$[M]\{\delta a\}=\{b\} \tag{B2}$$

where $[M]$ is the DVC Hessian matrix

$$\left\{\begin{array}{rcl}[M] & = & \displaystyle\int {}^{\mathrm{t}}\varphi\,{}^{\mathrm{t}}\boldsymbol{\nabla} f\boldsymbol{\nabla} f\varphi\,\mathrm{d}\boldsymbol{x}\\ \{b\} & = & \displaystyle\int {}^{\mathrm{t}}\varphi\,{}^{\mathrm{t}}\boldsymbol{\nabla} f\rho\,\mathrm{d}\boldsymbol{x}\end{array}\right. \tag{B3}$$

IDVC uses a more suited kinematic basis by integrating a model [37]. In the present case, the model presented in Appendix A is used. The parameters of the model, $\{p\}$ — or a normalisation, $\{\tilde{p}\}$, of them (see Appendix C) — are then the new unknowns of the problem. IDVC is thus an identification procedure. A convenient and lowly-intrusive way to integrate the model is to pass through the sensitivity field of the parameters

$$\{S_{\tilde{p}_i}\}=\frac{\partial\{a\}}{\partial\tilde{p}_i} \tag{B4}$$

$\{S_{\tilde{p}_i}\}$ is the displacement field induced by an incremental variation of $\tilde{p}_i$. A new Gauss-Newton procedure is set, solving at each iteration

$$ {}^{\mathrm{t}}[S][M][S]\{\delta\tilde{p}\} = {}^{\mathrm{t}}[S]\{b\} \tag{B5} $$

where $[S]$ is the concatenation of all the sensitivity fields.

Other measurement modalities can be integrated into the identification procedure. In the presented case, the force is also used. The increment, $\{\delta\tilde{p}\}$ is computed by solving

$$ \begin{aligned} [H]\{\delta\tilde{p}\} &= \{c\} \\ {}^{\mathrm{t}}\begin{bmatrix} S_a \\ S_F \end{bmatrix} \begin{bmatrix} \dfrac{M}{2\sigma_f^2} & 0_{(N\times 1)} \\ 0_{(1\times N)} & \dfrac{1}{\sigma_F^2} \end{bmatrix} \begin{bmatrix} S_a \\ S_F \end{bmatrix} \{\delta\tilde{p}\} &= {}^{\mathrm{t}}\begin{bmatrix} S_a \\ S_F \end{bmatrix} \begin{Bmatrix} \dfrac{b}{\sigma_f^2} \\ \dfrac{\Delta F}{\sigma_F^2} \end{Bmatrix} \end{aligned} \tag{B6} $$

where $[S_a]$ and $[S_F]$ are resp. the displacement and force sensitivity fields; σ_f the noise level of the images, σ_F, the uncertainty on the force; and ΔF, the difference between the measured force and the force computed with the current parameters $\{p\}$.

The thermal field is also considered in the identification procedure. Weak coupling is assumed because the strains are low in SiC/SiC composites. The measured temperature field — i.e. re-projected from the infrared images using the procedure detailed in [26] — is used as boundary conditions in the finite-element model.

The convergence criterion to reach stationarity is based on the norm, $\|\delta\tilde{p}\|$, of the increment of parameters. This norm should include the metric of the problem

$$ \|\delta\tilde{p}\| = \sqrt{{}^{\mathrm{t}}\{\delta\tilde{p}\}[H]\{\delta\tilde{p}\}} \tag{B7} $$

As $[H]$ is the inverse of the covariance matrix of $\tilde{p}$, if this norm is inferior to one, the variation of each parameter is inferior to its uncertainty (Appendix D). This criterion is generally stricter than a criterion on residual stationarity.

The computation of the sensitivity field is a time-consuming step. To speed up the IDVC convergence, the sensitivity field is not updated at each iteration. In between actual updates of all sensitivity fields (*outer iterations*), they are not updated for several *inner iterations*. Finding a good balance between outer and inner iterations allows for saving computation time. The criterion to update sensitivity fields is based on the gap between the parameter value (when the corresponding sensitivity was computed) and the current one.

In practice, sensitivity fields $[S_a]$ and $[S_F]$ are numerically computed using the sample finite element model and using Abaqus. The sensitivity field computation is parallelised. IDVC is performed using Correli[1], namely the computation of $[M]$ and $\{b\}$. The computations are performed on a Debian-Linux workstation with 24 cores and 250 Go of RAM. Inner iterations take about twenty seconds, and outer ones take ten minutes (using parallel computation for sensitivity fields).

C. Sensitivity study

The *sensitivity fields* are the displacement fields resulting from an infinitesimal change of one parameter, keeping all the others constant. As the parameters have different natures and dimensions, the sensitivity fields exhibit broadly distributed orders of magnitude. As the identification problem is ill-posed, when considering the original set of parameters $\{p\}$, this can lead to an ill-conditioning of $[H]$ (Eq. B6). A first step consists in normalising the parameters, such that the incremental variation of the normalised set of parameter $\{\tilde{p}\}$ induces sensitivity fields of the same orders of magnitude. The normalisation choices depend on the parameter natures and are given in Table C1.

Then, the eigenvalues and eigenvectors of $[H]$ should be studied. Eigenvectors provide information on the possible coupling between parameters. The components of the eigenvectors associated with the lowest eigenvalues have a very low contribution to the sensitivity field. In the considered configuration,

[1]Correli is LMPS's DIC and DVC toolbox.

nature	corresponding parameters, p_i	$\widetilde{p_i}$
modulus	E, E_{11}, E_{22}, G_{12}, G_{23}	$\dfrac{p_i}{p_{\mathrm{nom},i}}$
Poisson's ratio	ν, ν_{12}, ν_{23}	p_i
coefficient of thermal expansion	k, k_{11}, k_{22}	$\dfrac{\Delta T \ell}{u_{\mathrm{ref}}} p_i$

Table C1: Normalisation of the material parameters of the IDVC problem. ΔT is the temperature range of the test, u_{ref} is a reference displacement, and ℓ is a characteristic length (here, ℓ is the diameter of the sample).

they have an insignificant influence on the behaviour of the sample. That is why the two coefficients of thermal expansion of the tows are not considered in the identification.

It is also interesting to consider the sensitivity field for themselves. The sensitivities of the displacement field with respect to material properties are considered hereafter. To appreciate the influence of one parameter, some examples of sensitivity fields are shown in Figure C1. The corresponding sensitivity fields are relatively smooth even if the material properties are not spatially homogeneous. Sensitivities along the z-axis (S_z) have a very low magnitude for most parameters. Indeed, the boundary conditions constrain the sample displacement in this direction. In turn, S_z on those boundary conditions are very high.

From one parameter to the next, the intensity of the sensitivity field may vary by more than one order of magnitude. Moreover, some fields have a similar pattern (e.g. room-temperature E and high-temperature E) and are only distinguished by their intensity, leading to indetermination. Those two points result in very poor conditioning of the identification problem.

D. Uncertainty computation

If the images are submitted to white Gaussian noise of standard deviation σ_f and this noise is low compared to the grey level dynamics, the covariance of

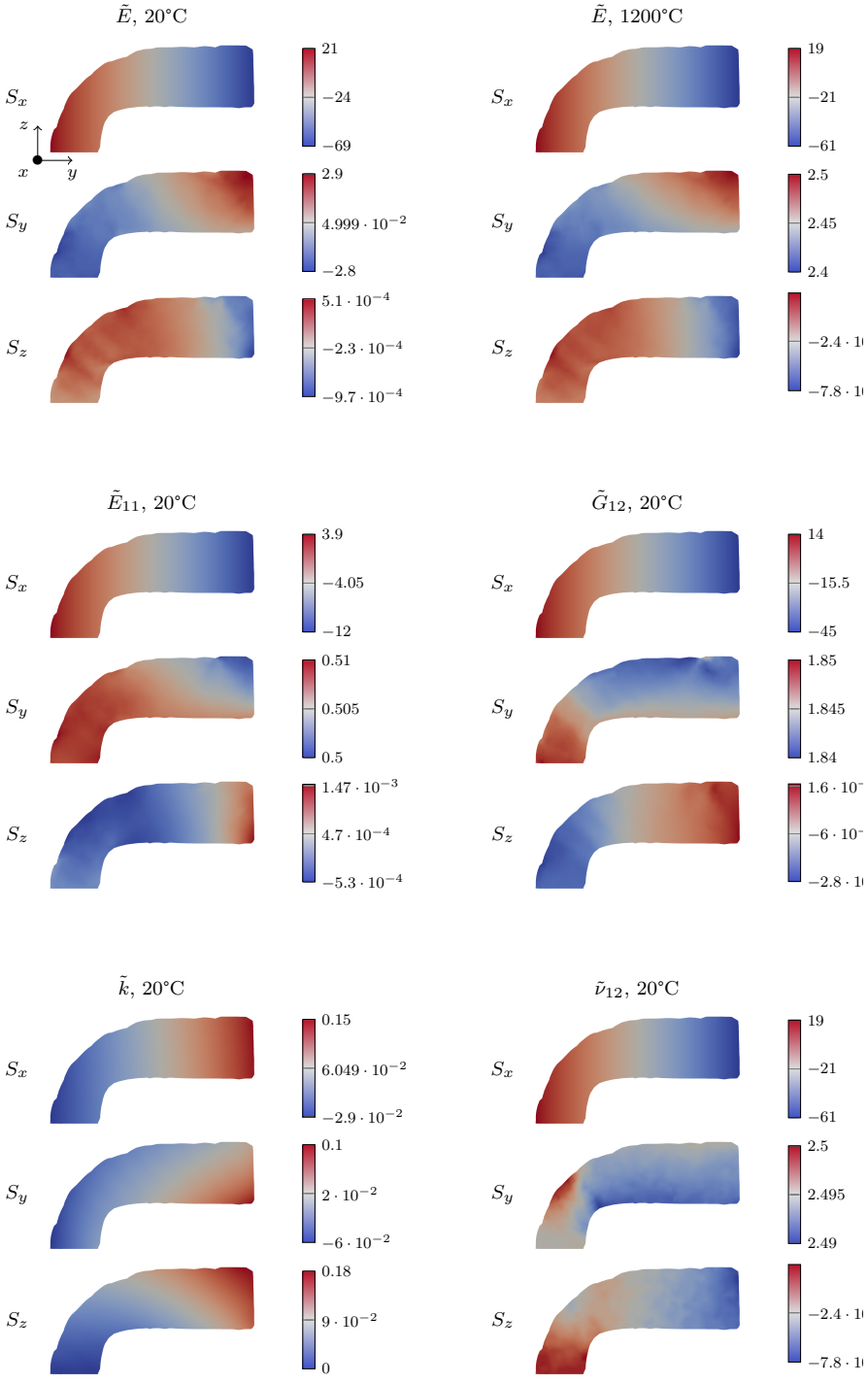

Figure C1: Some sensitivity fields cut in the median plane of the sample: displacement (µm) induced by a variation of the normalised parameters of 1%.

the displacement field, a, computed by DVC writes [38]

$$\langle \delta a \, {}^{\mathrm{t}} \delta a \rangle = 2\sigma_f^2 [M]^{-1} \tag{D1}$$

where $[M]$ is the DVC Hessian matrix (Eq. B3).

Excluding the model error, which is discussed in Section 4.1, the covariance of the parameters, $\tilde{p}$, is

$$\langle \delta \tilde{p} \, {}^{\mathrm{t}} \delta \tilde{p} \rangle = [H]^{-1} \tag{D2}$$

Indeed, the IDVC Hessian matrix $[H]$ already includes the noise level of the images, σ_f, and the uncertainty of the force, σ_F (Eq. B6). In this paper, the authors consider that the standard deviation of a parameter (i.e. the square root of the corresponding diagonal term of $[H]^{-1}$) is a good estimator of the uncertainty induced by the uncertainties in the experimental data. Those values are displayed in Table 1.

Data availability

The raw data required to reproduce these findings cannot be shared at this time due to legal reasons. The processed data required to reproduce these findings cannot be shared at this time due to the same reasons.

References

[1] R. Naslain, Design, preparation and properties of non-oxide CMCs for application in engines and nuclear reactors: An overview, Compos. Sci. Technol. 64 (2) (2004) 155–170. doi:10.1016/S0266-3538(03)00230-6.

[2] P. L. N. Murthy, N. N. Nemeth, D. N. Brewer, S. Mital, Probabilistic analysis of a SiC/SiC ceramic matrix composite turbine vane, Compos. Part B 39 (4) (2008) 694–703. doi:10.1016/j.compositesb.2007.05.006.

[3] F. Boussu, I. Cristian, S. Nauman, General definition of 3D warp interlock fabric architecture, Compos. Part B 81 (2015) 171–188. doi:10.1016/j.compositesb.2015.07.013.

[4] L. Turpin, S. Roux, O. Caty, A. King, S. Denneulin, É. Martin, In-situ tomographic study of a 3D-woven SiC/SiC composite part subjected to severe thermo-mechanical loads, J. Synchr. Rad. 29 (2022). doi:10.1107/S1600577522000406.

[5] F. W. Zok, Ceramic-matrix composites enable revolutionary gains in turbine engine efficiency, Am. Ceram. Soc. Bull. 95 (5) (2016) 22–28.

[6] V. Mazars, Etude des endommagements sur CMC par une approche de modélisation micro-méso alimentée par des essais in-situ, Ph.D. thesis, Univ. de Bordeaux (2018).

[7] Y. Zayachuk, P. Karamched, C. Deck, P. Hosemann, D. E. J. Armstrong, Linking microstructure and local mechanical properties in SiC-SiC fiber composite using micromechanical testing, Acta Mater. 168 (2019) 178–189. doi:10.1016/j.actamat.2019.02.001.

[8] S. V. Lomov, D. S. Ivanov, I. Verpoest, M. Zako, T. Kurashiki, H. Nakai, S. Hirosawa, Meso-FE modelling of textile composites: Road map, data flow and algorithms, Compos. Sci. Technol. 67 (9) (2007) 1870–1891. doi:10.1016/j.compscitech.2006.10.017.

[9] B. Wintiba, B. Sonon, K. Ehab Moustafa Kamel, T. J. Massart, An automated procedure for the generation and conformal discretization of 3D woven composites RVEs, Compos. Struct. 180 (2017) 955–971. doi:10.1016/j.compstruct.2017.08.010.

[10] N. Isart, B. El Said, D. Ivanov, S. Hallett, J. Mayugo, N. Blanco, Internal geometric modelling of 3D woven composites: A comparison between different approaches, Compos. Struct. 132 (2015) 1219–1230. doi:10.1016/j.compstruct.2015.07.007.

[11] A. Mendoza, J. Schneider, E. Parra, S. Roux, The correlation framework: Bridging the gap between modeling and analysis for 3D woven composites, Compos. Struct. 229 (2019) 111468. doi:10.1016/j.compstruct.2019.111468.

[12] Y. Wielhorski, A. Mendoza, M. Rubino, S. Roux, Numerical modeling of 3D woven composite reinforcements : A review, Compos. Part A (2022) 106729doi:10.1016/j.compositesa.2021.106729.

[13] Y. Liu, I. Straumit, D. Vasiukov, S. V. Lomov, S. Panier, Prediction of linear and non-linear behavior of 3D woven composite using mesoscopic voxel models reconstructed from X-ray micro-tomography, Compos. Struct. 179 (2017) 568–579. doi:10.1016/j.compstruct.2017.07.066.

[14] K. H. Khafagy, S. Datta, A. Chattopadhyay, Multiscale characterization and representation of variability in ceramic matrix composites, J. Compos. Mater. 55 (18) (2021) 2431–2441. doi:10.1177/0021998320978445.

[15] J. Bénézech, Modélisation aux échelles méso- et macroscopique du com-

portement mécanique de zones singulières de pièces de structure en CMC, Ph.D. thesis, Univ. de Bordeaux (2019).

[16] N. Naouar, E. Vidal-Sallé, J. Schneider, E. Maire, P. Boisse, Meso-scale FE analyses of textile composite reinforcement deformation based on X-ray computed tomography, Compos. Struct. 116 (2014) 165–176. doi:10.1016/j.compstruct.2014.04.026.

[17] E. Maire, J. Adrien, P. J. Withers, In-situ X-ray tomographic study of materials, MDPI, 2020.

[18] V. Mazars, O. Caty, G. Couégnat, A. Bouterf, S. Roux, S. Denneulin, J. Pailhès, G. L. Vignoles, Damage investigation and modeling of 3D woven ceramic matrix composites from X-ray tomography in-situ tensile tests, Acta Mater. 140 (2017) 130–139. doi:10.1016/j.actamat.2017.08.034.

[19] H. A. Bale, A. Haboub, A. A. Macdowell, J. R. Nasiatka, D. Y. Parkinson, B. N. Cox, D. B. Marshall, R. O. Ritchie, Real-time quantitative imaging of failure events in materials under load at temperatures above 1,600°C, Nature Mater. 12 (1) (2013) 40–46. doi:10.1038/nmat3497.

[20] B. K. Bay, Methods and applications of digital volume correlation, J. Strain Anal. Eng. Des. 43 (8) (2008) 745–760. doi:10.1243/03093247JSA436.

[21] F. Hild, A. Bouterf, L. Chamoin, H. Leclerc, F. Mathieu, J. Neggers, F. Pled, Z. Tomičević, S. Roux, Toward 4D mechanical correlation, Adv. Model. Simul. Eng. Sci. 3 (1) (2016). doi:10.1186/s40323-016-0070-z.

[22] A. Buljac, C. Jailin, A. Mendoza Quispe, J. Neggers, T. Taillandier-Thomas, A. Bouterf, B. Smaniotto, F. Hild, S. Roux, Digital volume correlation: Review of progress and challenges, Exp. Mech. 58 (5) (2018) 661–708. doi:doi.org/10.1007/s11340-018-0390-7.

[23] Y. Chen, L. Gélébart, C. Chateau, M. Bornert, A. King, P. Aimedieu, C. Sauder, 3D Detection and Quantitative Characterization of Cracks in

a Ceramic Matrix Composite Tube Using X-Ray Computed Tomography, Exp. Mech. 60 (3) (2020) 409–424. doi:10.1007/s11340-019-00557-5.

[24] S. Roux, F. Hild, Optimal procedure for the identification of constitutive parameters from experimentally measured displacement fields, Int. J. Solids Struct. 184 (2020) 14–23. doi:10.1016/j.ijsolstr.2018.11.008.

[25] T. Archer, M. Berny, P. Beauchêne, F. Hild, Creep behavior identification of an environmental barrier coating using full-field measurements, J. Eu. Ceram. Soc. 40 (15) (2020) 5704–5718. doi:10.1016/j.jeurceramsoc.2020.06.009.

[26] L. Turpin, S. Roux, O. Caty, S. Denneulin, Coupling tomographic and thermographic measurements for in-situ thermo-mechanical tests, Meas. Sci. Technol. 32 (2021) 035401. doi:10.1088/1361-6501/abcc9f.

[27] L. Turpin, S. Roux, O. Caty, S. Denneulin, A phase field approach to limited-angle tomographic reconstruction, Fundemanta Informaticae 172 (2020) 203–219. doi:10.3233/FI-2020-1901.

[28] H. Carpentier, O. Caty, Y. Le Petitcorps, E. Maire, A. Marchais, N. Eberling-Fux, G. Couégnat, In situ observation of the capillary infiltration of molten silicon in a sic/sic composite by x-ray radiography, J. Eu. Ceram. Soc. 42 (5) (2022) 1947–1954. doi:10.1016/j.jeurceramsoc.2021.12.041.

[29] S. Sakaguchi, N. Murayama, Y. Kodama, F. Wakai, The Poisson's ratio of engineering ceramics at elevated temperature, J. Mater. Sci. Lett. 10 (5) (1991) 282–284. doi:10.1007/BF00735658.

[30] S. K. Mital, B. A. Bednarcyk, S. M. Arnold, J. Lang, Modeling of melt-infiltrated SiC/SiC composite properties, Tech. rep., NASA/TM (2009).

[31] F. Hild, S. Roux, Digital image correlation: From displacement measurement to identification of elastic properties — A Review, Strain 42 (2006) 69–80. doi:10.1111/j.1475-1305.2006.00258.x.

[32] P. Galizia, D. Sciti, Disclosing residual thermal stresses in uht fibre-reinforced ceramic composites and their effect on mechanical behaviour and damage evolution, Compos. Part B 248 (2023) 110369. doi:https://doi.org/10.1016/j.compositesb.2022.110369.

[33] L. Gélébart, C. Colin, Effects of porosity on the elastic behaviour of CVI SiC/SiC composites, J. Nucl. Mater. 386-388 (C) (2009) 82–85. doi:10.1016/j.jnucmat.2008.12.064.

[34] J. Bénézech, G. Couégnat, Variational segmentation of textile composite preforms from X-ray computed tomography, Compos. Struct. 230 (2019) 111496. doi:10.1016/j.compstruct.2019.111496.

[35] P. Alliez, C. Jamin, L. Rineau, S. Tayeb, J. Tournois, M. Yvinec, 3D mesh generation, in: CGAL user and reference manual (5.1), 2020.
URL https://doc.cgal.org/5.1/Manual/packages.html#PkgMesh3

[36] S. Roux, F. Hild, P. Viot, D. Bernard, Three-dimensional image correlation from X-ray computed tomography of solid foam, Compos. Part A 39 (8) (2008) 1253–1265. doi:10.1016/j.compositesa.2007.11.011.

[37] M. Bertin, F. Hild, S. Roux, F. Mathieu, H. Leclerc, P. Aimedieu, Integrated digital image correlation applied to elastoplastic identification in a biaxial experiment, J. Strain Anal. Eng. 51 (2) (2016) 118–131. doi:10.1177/0309324715614759.

[38] S. Roux, F. Hild, Stress intensity factor measurements from digital image correlation: Post-processing and integrated approaches, Int. J. Fract. 140 (2006) 141–157. doi:10.1007/s10704-006-6631-2.